Evaluation of the reliability of resistance spot welding control via on-line monitoring of dynamic resistance

Sergey Butsykin[1,2] · Anton Gordynets[2] · Alexey Kiselev[2] · Mikhail Slobodyan[3]

Abstract

In resistance spot welding (RSW), initial resistance between electrodes (RBE) determines heat input (according to Joule's law) and greatly affects the quality of joints. In turn, RBE values are characterized by substantial uncertainty and vary during the RSW processes. To reduce their dispersions, preliminary low-current pulses are applied. In some cases, the quality of the formed RSW joints are controlled using dynamic resistances obtained by feedback from advanced power sources. In these studies, the effect of four preheating current diagrams on the stabilization of the RBE values was investigated for a wide range of parts made of copper, brass, bronze, austenitic stainless steel, as well as aluminum, titanium and zirconium alloys with thicknesses from 0.2 to 1.0 mm in various combinations. Also, the RSW process control capabilities were assessed using feedback from an up-to-date digital synthesizer of unipolar current pulses. As a result, the RBE values were stabilized in all studied cases. Ranges of the variations between the maximum and minimum RBE values decreased from about 5–11 down to 2–5 times. However, the applied algorithms of the preheating current pulses had no effect on the RBE dispersions. It was found that dynamic electrical processes in a welding gun cause distortion of actual RBE curves, which makes it difficult to control heat input and, respectively, the formation of weld nuggets.

Introduction

A brief historical background on the development of the control concepts for resistance spot welding

Resistance spot welding (RSW) has been used in many industries since the early twentieth century. In the 1930s, the key patterns of the formation of weld nuggets have been already determined, as well as various types of welding equipment have been developed and deployed. Conventional RSW procedures have satisfied the required quality level in mass production for decades (Paton & Lebedev, 1969). However, welded structures are becoming more and more complex, and their operating conditions are turning more and more severe. In addition, designing new steels and alloys determines the demand for advanced RSW procedures that enable to join parts with the highest quality (Ahmed et al., 2021; Aufiqur-rahman et al., 2021; Lee & Chang, 2020; Liu & Wei, 2020; Piott et al., 2020; Şahin et al., 2021; Zhang et al., 2020a, 2020b), especially in critical structures.

✉ Mikhail Slobodyan
s.m.s@ngs.ru

Sergey Butsykin
butsykin.s.e@gmail.com

Anton Gordynets
mnet@inbox.ru

Alexey Kiselev
tskweld@mail.ru

[1] 'Polyus' Research and Production Center, 56v Kirov Avenue, Tomsk 634050, Russia

[2] Tomsk Polytechnic University, 30 Lenin Avenue, Tomsk 634050, Russia

[3] Tomsk Scientific Center SB RAS, 10/4 Akademicheskii Prospect, Tomsk 634055, Russia

Currently, challenges of continuous improvement of the quality of manufactured products are being solved within the framework of the Industry 4.0 concept (Lasi et al., 2014; Lee et al., 2015). This strategic initiative is aimed at creating intelligent factories with advanced manufacturing technologies embedding cyber-physical systems, internet of things, and cloud computing. According to Zhong et al. (2017), intelligent manufacturing processes '*are able to monitor physical processes, create a so-called 'digital twin' (or 'cyber twin') of the physical world, and make smart decisions through real-time communication and cooperation with humans, machines, sensors, and so forth*'. In these cases, product life cycles are facilitated using smart sensors, adaptive decision-making models, advanced materials, intelligent devices, and data analytics (Li et al., 2017). With regard to RSW, the following patterns have to be considered. The feature of the formation of weld nuggets is the inability to visually control both processes and results without destructive tests. In addition, it is not always possible to apply non-destructive testing methods due to the peculiarities of shapes of welded structures and/or their small dimensions.

Based on the above-mentioned issues, some attempts to develop and implement methods for predicting the quality of weld nuggets using feedback from various sensors have been made for more than half a century. The first detailed descriptions of some of the obtained results, known to the authors, have been published in the monograph by Paton and Lebedev (1969). Relatively recent advances in this field are summarized in a review by Zhou and Yao (2019). Nevertheless, many efforts for improving different online RSW controlling procedures are being made by numerous researchers based on various physical phenomena at the present time. In particular, the investigated criteria have been dynamic resistance (Batista et al., 2020; Zeng et al., 2020; Zhou et al., 2020; Zhao, Bezgans et al., 2021; Zhou et al., 2021; Zhou et al., 2022a, 2022b), electrical energy and force between the electrodes (Batista et al., 2020), displacement of electrodes (Xia et al., 2020, 2021; Zhou et al., 2021), infrared thermal image processing results (Hernández et al., 2020), images of electrode prints (Dai et al., 2021; Younes et al., 2020), ultrasonic and acoustic emission signals (Dejans et al., 2021; Ghafarallahi et al., 2021; Ji et al., 2021), etc. To increase the reliability of these predictions, artificial intelligence algorithms have been applied (machine learning (Tercan & Meisen, 2022; Zhou et al., 2022a, 2022b) and neural networks (Pashazadeh et al., 2016; Xiao et al., 2022), as exampes). With all the indisputable achievements in the mentioned attempts to implement the real-time RSW controlling procedures, there are many open questions about the consistency of the big data processing results with the real physical processes to be controlled. As highlighted by Zhou and Yao (2019) in their review, '*The effect of* [RSW] *process analysis is limited because methods lack physical support*.' In this regard, filling the gap in knowledge about the relationship between the recorded values of measured indirect parameters and the possibility of controlling production procedures in accordance with the intelligent manufacturing framework (Zhong et al., 2017) remains relevant.

Methods for Stabilizing Heat Unput in Resistance Spot Welding that Determines the Quality of Joints

One more topical research direction is the control of the RSW processes by programming heat input algorithms (Akbolatov et al., 2019; Gnyusov et al., 2005; Kiselev & Slobodyan, 2019; Klimenov et al., 2020; Lee & Chang, 2020; Pashazadeh et al., 2016; Slobodyan & Kiselev, 2019; Soomro et al., 2021; Stadler et al., 2021; Wang et al., 2020; Zhang et al., 2020a, 2020b) or electrode force dynamics (Wohner et al., 2021). This is especially true for steels and alloys that tend to form quenching microstructures and internal discontinuities (especially cracks). In these cases, functional properties of the joints depend not only on the weld nugget sizes, but also on the microstructures of the metal and the heat-affected zone, as well as the presence of discontinuities. The developed approach is based on the well-known fact that a sound RSW joint can be obtained only with the optimal dynamics of changes in these parameters over time, allowing to melt a nugget of the required dimensions without expulsions and other defects. Respectively, the RSW process control should include presetting, as well as real-time monitoring and (if possible) adjusting current, voltage and electrod force values. They directly determine the heat input algorithms in accordance with Joule's laws discussed below (it should be noted that resistance is the ratio of voltage to current at any given moment according to Ohm's law).

As mentioned above, the functional properties of the RSW joints depend on the heat input algorithm, parameters of the parts to be welded (materials, thicknesses, surface conditions, etc.), as well as electrode tip shapes and force. These dependences are characterized by complexity and significant uncertainty. Nevertheless, it is known that heat input Q is generated upon current I is flowing through resistance between electrodes (RBE) R during time t according to Joule's law:

$$Q = \int_0^t I^2(t)R(t)dt \qquad (1)$$

The first variable, namely the current level as a function of time, can be controlled with advanced power sources based on digital signal processors, while the second one (the RBE value depending on many factors discussed below) is extremely difficult to predict and to control in RSW processes. Early researchers in this area has proposed significant

simplifications for estimating the RBE values. For example, the key role of heat generation is assigned to the bulk metal resistance according to Orlov (1975):

$$R = \rho \cdot \frac{2 \cdot \delta}{S_c}, \tag{2}$$

where ρ is the specific electrical resistance of the welded metal, δ is the thicknesses of the similar joined work-pieces, S_c is the cross-sectional area of the work-pieces through which welding current flows.

Sokolov (1971) has agreed with Eq. (2), but has supplemented it by the k current spreading coefficient:

$$R = k \cdot \rho \cdot \frac{2\delta}{S_c} \tag{3}$$

Such simplified relationships, as well as more advanced formulas with many variables studied by Akbolatov et al. (2019), cannot be implemented for both developing RSW procedures and controlling these processes, especially according to the above-mentioned intelligent manufacturing framework (Zhong et al., 2017). In real cases, an RBE value consists of the bulk resistances of parts to be welded, the contact resistances between the parts and electrodes, as well as one directly between the parts. It should be noted that all these components vary in the RSW process. The greatest contribution to the dispersion of RBE values is made by the initial contact resistances, which depend on the following factors:

- material of the electrodes, their tip shapes and force;
- materials and thicknesses of the parts to be welded;
- conditions of the contacting surfaces;
- wear degree of a welding gun, etc.

A great number of actually possible combinations of these factors is one of the main reasons for the instability of heat input and, as a consequence, the functional properties of welded joints. This is largely due to the variation in thicknesses, surface conditions and distortion of the welded parts, as well as degradation of electrodes and changes in the squeezing force due to unstable performance of pneumatic welding guns. To assess the effect of the above parameters on RBE values, variations of which during RSW have been studied for several decades, many models of electrical contacts have been developed (Holm, 1981; Merl, 1962; Usov, 1963). The results of their analysis and verification using parts made of the Zr-1Nb alloy 0.25 + 0.25 mm and the 321 austenitic stainless steel 0.3 + 0.3 mm have been reported by Akbolatov et al. (2019). Discrepancies between the calculated and experimental data has been found in all studied cases.

To reduce the dispersion of RBE values and, accordingly, to stabilize heat input in the RSW process, it is proposed to preheat welding zones with preliminary low current pulses (Brechelt et al., 2019; Paton & Lebedev, 1969). In this case, microroughnesses are deformed and oxide films are fractured on metal surfaces, which causes enlargement of actual contact areas (Holm, 1981; Merl, 1962; Usov, 1963). As a result, the mean contact resistance values and their dispersion are recreased. In turn, this reduces the instability of heat input and the likelihood of the formation of discontinuities such as expulsions, burn-through, and lack of penetration. An additional possibility to heat input control in the RSW process provides up-to-date advanced power sources (Akbolatov et al., 2019; Gnyusov et al., 2005; Kiselev & Slobodyan, 2019; Klimenov et al., 2020; Slobodyan & Kiselev, 2019; Wang et al., 2021), which enable to ensure preset current algorithms. This expands possibilities for improving the quality of welded joints and, accordingly, the reliability of fabricated structures. However, any clear recommendations on the optimal algorithms for the preheating pulses, depending on the parts to be welded, have not been published to date. Preliminary studies of four ones have been carried out by Akbolatov et al. (2019) using the parts made of the Zr–1Nb alloy (0.25 + 0.25 mm) and the 321 austenitic stainless steel (0.3 + 0.3 mm). The preheating current pulses have provided different heat input dynamics and, accordingly, heat distribution in the contacts due to thermal conductivity of the metals. The reported results have shown that the RBE stabilization capabilities have been significantly different for the investigated combinations. The most probable reason has been deviations in the chemical compositions and properties of oxide layers on these materials.

The current research motivation

Based on the highlighted progress in the development of the intelligent manufacturing framework (Zhong et al., 2017) in terms of its implementation in RSW welding procedures, the following dual goal of this research has been formulated by the authors. Its first part has been to deeper understand the effect of the preheating current diagrams on the stabilization of RBE values and, accordingly, heat input in RSW of a wider range of parts made of copper, brass, bronze, austenitic stainless steel, as well as aluminum, titanium and zirconium alloys with thicknesses from 0.2 to 1.0 mm in various combinations. Using robotic production lines, these materials are widely joined by RSW in various industries (Paton & Lebedev, 1969), uncluding the nuclear (Gnyusov et al., 2005; IAEA, 2008; Kiselev & Slobodyan, 2019; Slobodyan & Kiselev, 2019), chemical and aerospace (Collings, 1984; Hatch, 1984; Osintsev & Fedorov, 2004) ones. It should be noted that the investigated materials differ in the thermophysical properties of both bulk metals and oxide layers. The second

Table 1 Specifications of the IPTKM-10 power source

Parameter	Value
Pulse current (kA)	0.125–10.000
Current pulse duration (ms)	0–60
Discreteness of current control (A)	125
Discreteness of current pulse duration regulation (ms)	0.1

part of the research goal has been to assess the possibilities to reliably evaluate and control of heat input in the welding zone, which directly affect the stable quality of RSW joints, by measuring indirect parameters, namely current and voltage, followed by statistical processing of these data. The summarized results can be used for further improving RSW procedures implemented in production routs within the intelligent manufacturing framework (Zhong et al., 2017) of the Industry 4.0 concept (Lasi et al., 2014; Lee et al., 2015). The revealed dependences enable to more clearly understand the correlation of 'digital twins' of the RSW joints with their real-world counterparts, which greatly determine the integrity of numerous critical structures.

Materials and methods

A special welding facility (Akbolatov et al., 2019) was used for the experimental assessment of RBE values and the possibility of their stabilization by preheating current pulses. It included an 'IPTKM-10' power source and a modernized 'MTT-02' welding gun. The 'IPTKM-10' power source was a digital synthesizer of unipolar current pulses with required algorithms regardless of the load resistance. Its specification is presented in Table 1. A 'RIGOL MSO 1074' digital oscilloscope and an active resistance (Akbolatov et al., 2019) were used to measure actual both current and voltage values. The experimental facility is shown in Fig. 1 with an example of industrial deployment of such up-to-date power sources as a part of robotic production lines for intelligent manufacturing of nuclear fuel assemblies.

Dome-shaped electrodes were made of the Cu-1Cr-0.05Zr bronze. Their dome radius was 20 mm; electrode force was 300 N. These values were the average ones of the previously studied ranges applied in mass industrial production. It should be noted that there was no correlation between these parameters and the RBE values in the early cases studied. Preheating current diagrams are shown in Fig. 2. They varied in algorithms of current rise: discrete (modes 1 and 2) and stepwise (modes 3 and 4), as well as sharp (Fig. 2a), and smooth with longer upslope (Fig. 2b). Their integral heat input was

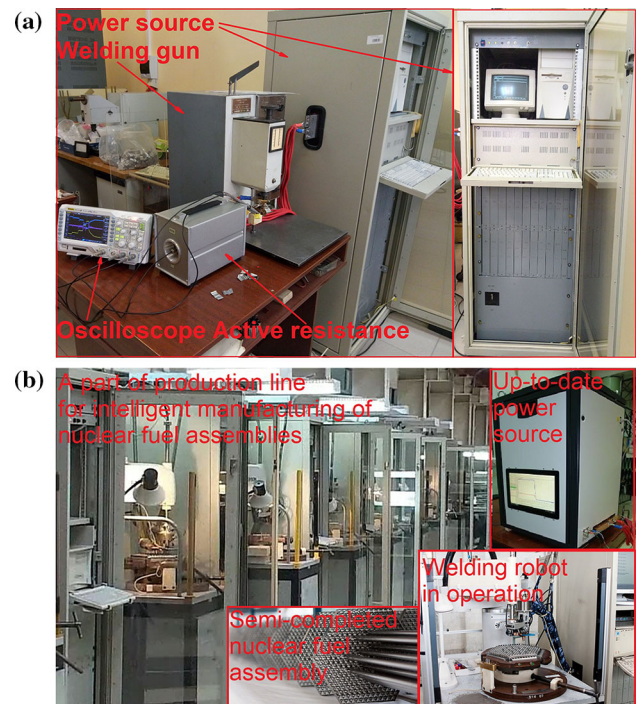**Fig. 1** The experimental facility (**a**) and an example of industrial deployment of such up-to-date power sources as a part of robotic production lines for intelligent manufacturing of nuclear fuel assemblies (**b**)
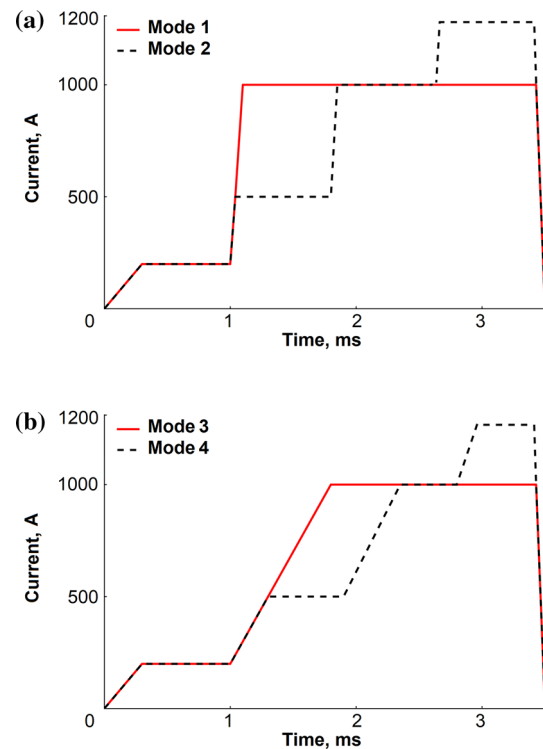

Fig. 2 Preheating pulses with discrete (modes 1 and 3) and stepwise (modes 2 and 4) current rise: **a** sharp increase, **b** smooth increase with longer upslope

Table 2 Combinations of the studied parts

	Al-6Mg alloy 1.0 mm	Copper 0.8 mm	CuBe2NiTi bronze 0.2 mm	CuBe2NiTi bronze 0.5 mm	CuZn37 brass 0.2 mm	CuZn37 brass 0.4 mm	Stainless steel 0.3 mm	Stainless steel 0.5 mm	Stainless steel 0.8 mm	Ti-0.8Al-0.8Mn alloy 0.5 mm	Zr-1Nb alloy 0.5 mm	Zr-1Nb alloy 0.8 mm
Al-6Mg alloy 1.0 mm	■	■										
Copper 0.8 mm	■	■				■						
CuBe2NiTi bronze 0.2 mm			■	■								
CuBe2NiTi bronze 0.5 mm			■	■								
CuZn37 brass 0.2 mm					■	■						
CuZn37 brass 0.4 mm		■			■	■						
Stainless steel 0.3 mm							■	■	■			
Stainless steel 0.5 mm							■	■	■			
Stainless steel 0.8 mm							■	■	■			
Ti-0.8Al-0.8Mn alloy 0.5 mm										■	■	
Zr-1Nb alloy 0.5 mm										■	■	■
Zr-1Nb alloy 0.8 mm											■	■

about the same. The parts were not welded in all investigated cases.

Combinations of the investigated materials and thicknesses are presented in Table 2; their chemical compositions are shown in Table 3 based on the data from the standards: GOST 18175 (1978); GOST 19,807 (1991); GOST 4784 (1997); GOST 859 (2001); GOST 15527 (2004); GOST 58175 (2014); TU 95.166 (1998). The main physical properties, affecting the results of these studies, are summarized in Table 4 based on reference books by Zaimovsky et al. (1981); Collings (1984); Hatch (1984); Osintsev and Fedorov (2004); IAEA (2008). Specific electrical resistances and melting points of the main possible oxides on the studied materials are presented in Table 5 according to Merl (1962); Usov (1963); Samsonov (1973); Lazarev et al. (1983).

Immediately before investigations, the surfaces of all parts were thoroughly cleaned sequentially with the P100 (a grit size of 125–160 µm), P240 (50–63 µm), and P600 (20–28 µm) sandpapers to remove main parts of oxide films and unify their roughness. Then, the samples were washed with running hot water, dried and degreased with ethyl alcohol.

To determine RBE values, actual current and voltage values were measured 200 times for each combination of the parts. The surfaces had been moved relative to each other every time so their different parts were in contact. The RBE levels were calculated using the data on measured current and

voltage values according to Ohm's law. Then, the data were statistically processed using *MS Excel*. Firstly, the dynamic resistance curves were smoothed by the three-point method (Akbolatov et al., 2019). Then, the initial RBE values were estimated in ~ 0.5 ms after turning on current of ~ 125 A to complete the transient processes in the secondary circuit, and the preheated RBE values were evaluated immediately before current was switched off (~ 3.5 ms in accordance with the current diagrams shown in Fig. 2). Dispersions of the RBE levels were assessed by their absolute values (maximum, mean, minimum) for each combination of the parts and preheating current pulses, as well as using both 'standard deviation' (*SD*) and 'mean absolute deviation' (*MAD*) statistical functions (Smith, 2018) according to the expressions (4) and (5), respectively:

$$SD = \sqrt{\frac{\sum (x_i - \overline{x})^2}{n - 1}}, \tag{4}$$

$$MAD = \frac{\sum |x_i - \overline{x}|}{n}, \tag{5}$$

where n was the number of observations, x_i were the different observations from 1 to n, and $\overline{x}$ was the mean value. The minimum levels of the deviations indicated the most effective stabilization of the RBE values, which contributed to the best heat input control in the RSW process.

Table 3 Chemical compositions of the studied materials

Material	Element												
	Al	As	Be	Bi	C	Ca	Cr	Cu	Fe	H	Hf	Mg	Mn
Al-6Mg alloy	91.10–93.68		0.0002–0.0050					< 0.1	< 0.4			5.8–6.8	0.5–0.8
Copper (commercially pure)		< 0.002		< 0.001				> 99.9 (Cu + Ag)	< 0.005				
CuBe2NiTi bronze	> 0.15		1.85–2.10					96.75–97.85	> 0.15				
CuZn37 brass				> 0.002				62–65	> 0.2				
Stainless steel (Grade 321)					< 0.12		17.0–19.0	< 0.4	Bal				< 2.0
Ti–0.8Al–0.8Mn alloy	1.5–2.5				> 0.1				> 0.3	> 0.012			0.7–2.0
Zr–1Nb alloy					< 0.0002	< 0.0001	< 0.0002		< 0.0005		< 0.0005		

Material	Element																Ref
	Mo	N	Nb	Ni	O	P	Pb	S	Sb	Si	Sn	Ti	V	W	Zn	Zr	
Al-6Mg alloy										< 0.4		0.02–0.10			< 0.2		GOST 4784, (1997)
Copper (commercially pure)				< 0.002	< 0.05		< 0.005	< 0.004	< 0.002		< 0.002				< 0.004		GOST 859, (2001)
CuBe2NiTi bronze				0.2–0.4			> 0.005	> 0.005		> 0.15		0.10–0.25					GOST 18,175, (1978)
CuZn37 brass						> 0.01	> 0.07		> 0.005						34.22–37.50		GOST 15,527, (2004)
Stainless steel (Grade 321)	< 0.5			9–11		< 0.035		< 0.02		< 0.8		< 0.8	< 0.2	< 0.2			GOST 58,175, (2014)
Ti–0.8Al–0.8Mn alloy		> 0.05			> 0.15					> 0.12		94.33–97.50				> 0.3	GOST 19,807, (1991)
Zr–1Nb alloy			0.9–1.1		< 0.001					< 0.0002						Bal	TU 95,166, (1998)

Table 4 Main physical properties of the studied materials

Parameter	Al–6Mg alloy (Hatch, 1984)	Copper (Osintsev & Fedorov, 2004)	CuZn37 brass (Osintsev & Fedorov, 2004)	CuBe$_2$NiTi bronze (Osintsev & Fedorov, 2004)	Cu-1Cr-0.05Zr bronze (Osintsev & Fedorov, 2004)	Stainless steel 321 (IAEA, 2008)	Ti-0.8Al-0.8Mn alloy (Collings, 1984; Holm, 1981)	Zr-1Nb alloy (IAEA, 2008; Zaimovsky et al., 1981)
Specific electrical resistance at 20 °C, 10^{-8} Ω m	6.73	1.724	~ 7	~ 9	2.04 to 3.76	71 to 75	~ 42	44 to 70
Temperature coefficient of electrical resistance at 20–100 °C	4.0×10^{-3}	4.3×10^{-3}					$\sim 3 \times 10^{-3}$	4.4×10^{-3}
Melting point, °C	650	1084	1060	1030	1080	1440	~ 1670	1837
Thermal conductivity at 20 °C, W m^{-1} K^{-1}	122	409	110	100	366	16	9.2	17 to 18
Heat capacity at 100 °C, kJ kg^{-1} K^{-1}	922	389	385	419		0.500	0.503	0.285 to 0.320
Thermal expansion coefficient at 20–100 °C, 10^{-6} K^{-1}	24.7	16.8	~ 20	16.5	17.5	~ 16	8.7	5.8
Hardness HB	65	35 to 110	68 to 155	90 to 400	52 to 130	180	200	200

Table 5 Specific electrical resistances and melting points of the main possible oxides on the studied materials

Oxide	Specific electrical resistance, $\Omega \cdot m$		Melting point, °C	Reference
	Cold (by default at 20 °C)	1000 °C		
Al_2O_3	10^{14}; 10^{16}; 3×10^{16}	5×10^6; 10^9	2050	Usov (1963), Samsonov (1973), Lazarev et al. (1983)
BeO	9×10^{11} (at 500 °C)	1.6×10^8	2520 to 2570	Samsonov (1973)
Cr_2O_3	10^{13}	40	1990; 2257 to 2427; 2334 ± 25	Usov (1963), Samsonov (1973), Lazarev et al. (1983)
CrO_2	1.2×10^{-2}		427	Samsonov (1973), Lazarev et al. (1983)
CrO_3			180 to 202	Samsonov (1973)
Cu_2O	$(1 \text{ to } 3) \times 10^6$; 10^8 to 10^9; 10^{10} to 10^{12}	1	1242 ± 5; ~ 1800 (dissociates)	Merl (1962), Usov (1963), Samsonov (1973), Lazarev et al. (1983)
CuO	10 to 10^3; 10^8; 10^9	0.10^{-3}; 10^2	1336; 1026 (dissociates)	Usov (1963), Samsonov (1973), Lazarev et al. (1983)
Cu_2O_3			100	Samsonov (1973)
$Fe_{0.947}O$	10^7 to 10^{10}		1374 ± 5	Samsonov (1973), Lazarev et al. (1983)
FeO	10^7 to 10^{10}	10^{-2}; 10^4	1420	Usov (1963), Samsonov (1973), Lazarev et al. (1983)
$FeO_{1.05}$	10^7 to 10^{10}		1371 ± 5	Samsonov (1973), Lazarev et al. (1983)
$FeO_{1.056}$	10^7 to 10^{10}		1374 ± 5	Samsonov (1973), Lazarev et al. (1983)
$FeO_{1.10}$	10^7 to 10^{10}		1388 ± 5	Samsonov (1973), Lazarev et al. (1983)
$FeO_{1.15}$	10^7 to 10^{10}		1406 ± 5	Samsonov (1973), Lazarev et al. (1983)
$FeO_{1.20}$	10^7 to 10^{10}		1424 ± 5	Samsonov (1973), Lazarev et al. (1983)
Fe_3O_4	10^{-2}; 0.4	2.2	1583 ± 2; 1594 ± 2; 1597 ± 2	Samsonov (1973), Lazarev et al. (1983)
Fe_2O_3	10^7 to 10^{10}	82	1350; 1562	Samsonov (1973), Lazarev et al. (1983)
MgO	10^{14} to 10^{15} (at 300 °C)	6×10^8	2800	Usov (1963), Samsonov (1973)
MnO	10^{10}; 10^{11} to 10^{17}		1785 ± 15; 1842 ± 10	Samsonov (1973), Lazarev et al. (1983)
Mn_3O_4	10^6 to 10^8	1.43×10^3	1560 ± 10	Samsonov (1973), Lazarev et al. (1983)
Mn_2O_3	10^6 to 10^8		1347	Samsonov (1973), Lazarev et al. (1983)
MnO_2	1 to 10^4		847	Samsonov (1973), Lazarev et al. (1983)
Mn_2O_7			6 ± 1	Samsonov (1973)
Nb_4O			350	Samsonov (1973)
NbO			1940 ± 15; 2377	Samsonov (1973)

Table 5 (continued)

Oxide	Specific electrical resistance, $\Omega \cdot m$		Melting point, °C	Reference
	Cold (by default at 20 °C)	1000 °C		
Nb_2O_3			1772	Samsonov (1973)
NbO_2			2080 ± 20	Samsonov (1973)
Nb_2O_5	2×10^{-3}	8	1490 ± 20	Samsonov (1973)
NiO	10^{10}; 10^{13}; 10^{17}	1.4×10^2; 10^4	1552; 1957 ± 20; 2090	Usov (1963), Samsonov (1973), Lazarev et al. (1983)
Ni_2O_3	10^6	–	~ 300 (dissociates)	Usov (1963)
Ti_3O			1940 ± 30	Samsonov (1973), Lazarev et al. (1983)
TiO	3.1×10^{-2}; 6×10^4		1750 to 2020	Samsonov (1973), Lazarev et al. (1983)
Ti_2O_3	0.1		1900 to 2130	Samsonov (1973)
Ti_3O_5			1774 ± 20; 2177	Samsonov (1973), Lazarev et al. (1983)
TiO_2	3×10^7 (at 500 °C); 10^{15}	5×10^4	1870 ± 15; 1850 ± 20	Samsonov (1973), Lazarev et al. (1983)
TiO_3			670	Samsonov (1973)
ZnO	(6 to 9) $\times 10^6$; 10^9; 9.44×10^3 (at 150 °C)	2.6; 10^2	~ 1800 (sublimes); 1975	Usov (1963), Samsonov (1973), Lazarev et al. (1983)
Zr_6O			1940 ± 30	Lazarev et al. (1983)
Zr_3O			1975 ± 30	Samsonov (1973), Lazarev et al. (1983)
ZrO_2	3×10^6 (at 300 °C)	10^3	2900; 2700 ± 25	Samsonov (1973), Lazarev et al. (1983)

In addition, correlation coefficients ρ_{XY} were used to assess the strength and direction of the linear relationship between the following (*X* and *Y*) parameters: the calculated mean bulk resistance values at room temperature and the experimentally determined RBE ones, as well as between the deviations of the preheated RBE values and the current modes grouped by similar materials. For these purposes, the typical expression was applied (Smith, 2018):

$$\rho_{XY} = \frac{cov(X, Y)}{SD_X SD_Y}, \tag{6}$$

where *cov(X, Y)* was their covariance (a measure of the joint variability); SD_X and SD_Y were their standard deviations. The results were interpreted in accordance with the theory of statistics: (1) the larger were their absolute values in the range from -1 to $+1$, the stronger were the relationships between the variables, and (2) the sign of the coefficients indicated the directions of the relationships (if the coefficients were positive then both variables increased or decreased together; in another case, one variable enhanced as the other reduced).

Results

Experimentally obtained current and voltage values, as well as calculated dynamic Resistances

Typical experimentally measured current and voltage curves, as well as calculated dynamic resistance ones are shown in Fig. 3 for the studied current profiles and materials. Their comparison enabled to assert that the type of dynamic resistances depended not only on the current profiles, but also on the electrical properties of the materials (Table 4), as well as components of possible surface layers (in particular, oxides according to Table 5). For most of the studied cases, the RBE values decreased upon heating due to current flow (Fig. 3a, c, d). However, the results of heating copper and its alloys (both bronze and brass) did not always correspond to this pattern. In some cases (for example, Fig. 3b), the RBE levels increased upon heating due to both extremely low values of initial contact resistances and an increase in bulk electrical resistivity. It should be noted that dynamic electrical processes had been in a welding gun, besides transient ones after sharp changes in current. As a result, current and voltage had been in antiphase that caused distortion of the calculated
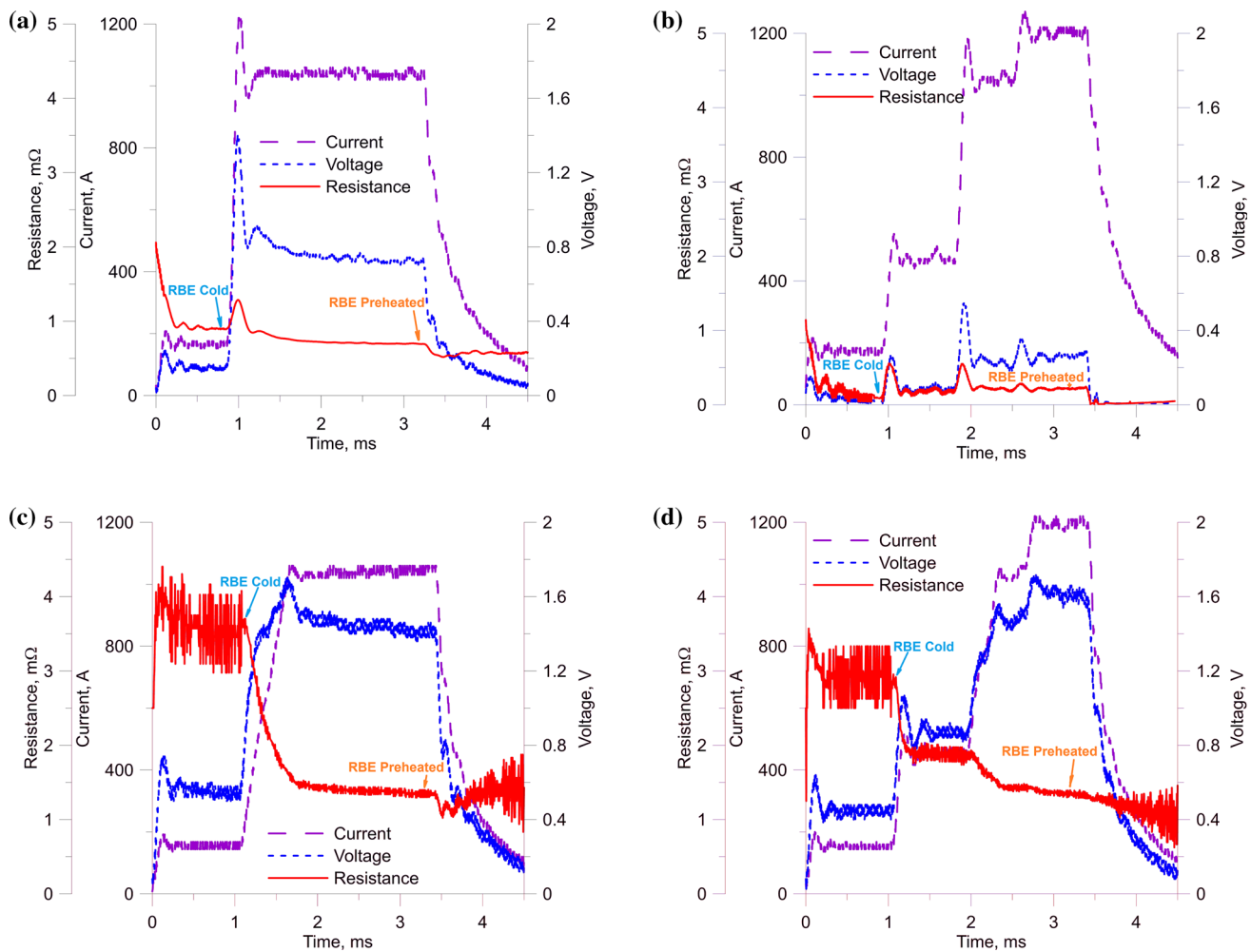
Fig. 3 Typical measured current and voltage as well as calculated dynamic resistances: **a** mode 1, Al–6Mg 0.1 mm + Al–6Mg 0.1 mm; **b** mode 2, Copper 0.8 mm + Copper 0.8 mm; **c** mode 3, Stainless steel 0.5 mm + Stainless steel 0.5 mm; **d** mode 4, Zr–1Nb 0.8 mm + Zr–1Nb 0.8 mm

RBE curves, which made it difficult to assess their actual values. This tendency worsened with raising the RBE level.

Statistically processed data

The results of statistical processing of both cold and pre-heated RBE values are presented in Table 6 and visualized in Fig. 4. Due to the large number of axes (eight dozen) on radar charts in Fig. 4, the legend of their designations is presented separately in Table 7. For comparison, the calculated bulk resistance values of the parts are reported in Table 6 as well. The analysis of these data enabled to draw a conclusion that, in general, there was a correspondence of the minimum, mean and maximum RBE values (both cold and preheated) to specific electrical resistances of the parts at room temperature, the level of which was approximately four orders of magnitude lower. The fact was confirmed by the calculated correlation coefficients between these parameters, the values

of which ranged from 0.86 to 0.89. Nevertheless, the correlation coefficients between the specific electrical resistances of the parts and the variance of the cold RBE values (Table 8) were significantly lower than the above-mentioned ones (0.74 for SD and 0.73 for MAD). The specific electrical resistance levels of the parts did not affect the variance of the preheated RBE values at all, since the correlation coefficients were only 0.46 and 0.45 for SD and MAD, respectively. Based on these data, an additional conclusion could be drawn that the SD statistical function more reliably reflected the actual variance of the RBE values than the MAD one.

In general, all studied preheating pulses had a positive effect on the RBE stabilization. After current flowing, the range of the dispersions between the maximum and minimum RBE values significantly decreased from about 5–11 down to 2–5 times (Table 9). However, the influence of the investigated algorithms of the preheating current pulses on the RBE stabilization was not observed. The correlation coefficients between the used current modes and the variations

Table 6 The RBE values and their deviations

Parts		Al–6Mg 1.0 mm + Al–6Mg 1.0 mm				Al–6Mg 1.0 mm + Copper 0.8 mm				Copper 0.8 mm + Copper 0.8 mm				CuBe$_2$NiTi bronze 0.2 mm + CuBe$_2$NiTi bronze 0.2 mm				CuBe$_2$NiTi bronze 0.2 mm + CuBe$_2$NiTi bronze 0.5 mm			
Calculated mean bulk resistance at 20 °C, 10^{-10} Ω		1.35				0.81				0.28				0.36				0.63			
Current modes		1	2	3	4	1	2	3	4	1	2	3	4	1	2	3	4	1	2	3	4
RBE cold, mΩ	Max	2.12	2.52	4.43	4.39	1.12	1.62	1.70	1.59	0.66	0.70	0.80	0.68	0.45	0.55	0.44	0.39	0.82	1.03	1.30	1.12
	Mean	1.06	1.28	2.45	2.16	0.59	1.01	0.83	1.03	0.29	0.37	0.35	0.35	0.27	0.32	0.32	0.31	0.46	0.56	0.48	0.63
	Min	0.62	0.70	0.89	0.75	0.31	0.68	0.50	0.69	0.16	0.21	0.19	0.22	0.16	0.18	0.21	0.22	0.26	0.31	0.22	0.34
RBE preheated, mΩ	Max	0.84	0.90	0.99	1.01	0.54	0.54	0.64	0.54	0.29	0.30	0.36	0.33	0.22	0.35	0.31	0.30	0.42	0.43	0.47	0.49
	Mean	0.57	0.78	0.79	0.83	0.39	0.48	0.51	0.47	0.20	0.24	0.25	0.25	0.17	0.23	0.24	0.24	0.29	0.34	0.33	0.39
	Min	0.69	0.62	0.64	0.69	0.28	0.39	0.42	0.42	0.15	0.17	0.17	0.21	0.14	0.14	0.18	0.21	0.22	0.27	0.21	0.28
Cold	SD	0.32	0.39	0.75	0.78	0.16	0.19	0.23	0.19	0.08	0.10	0.10	0.08	0.06	0.07	0.04	0.04	0.14	0.17	0.15	0.18
	MAD	0.25	0.32	0.63	0.65	0.13	0.15	0.18	0.15	0.06	0.08	0.07	0.06	0.04	0.05	0.04	0.03	0.12	0.13	0.11	0.15
Preheated	SD	0.06	0.06	0.06	0.06	0.06	0.03	0.04	0.03	0.03	0.03	0.04	0.03	0.01	0.05	0.03	0.02	0.05	0.04	0.05	0.05
	MAD	0.05	0.04	0.05	0.05	0.05	0.03	0.03	0.02	0.02	0.02	0.03	0.02	0.01	0.04	0.02	0.01	0.04	0.03	0.04	0.04

Parts		CuBe$_2$NiTi bronze 0.5 mm + CuBe$_2$NiTi bronze 0.5 mm				CuZn37 brass 0.2 mm + CuZn37 brass 0.2 mm				CuZn37 brass 0.2 mm + CuZn37 brass 0.4 mm				CuZn37 brass 0.4 mm + CuZn37 brass 0.4 mm				CuZn37 brass 0.4 mm + Copper 0.8 mm			
Calculated mean bulk resistance at 20 °C, 10^{-10} Ω		0.90				0.28				0.42				0.56				0.42			
Current modes		1	2	3	4	1	2	3	4	1	2	3	4	1	2	3	4	1	2	3	4
RBE cold (mΩ)	Max	0.46	0.44	0.67	0.84	0.54	0.50	0.33	0.33	0.43	0.52	0.46	0.37	0.40	0.45	0.34	0.32	0.92	0.86	0.52	0.64
	Mean	0.34	0.34	0.38	0.45	0.31	0.26	0.21	0.22	0.27	0.25	0.25	0.26	0.22	0.24	0.22	0.20	0.38	0.38	0.29	0.35
	Min	0.23	0.27	0.25	0.31	0.18	0.13	0.12	0.14	0.15	0.16	0.16	0.19	0.13	0.17	0.14	0.13	0.14	0.18	0.16	0.20
RBE preheated (mΩ)	Max	0.33	0.34	0.42	0.45	0.25	0.22	0.17	0.18	0.23	0.27	0.31	0.26	0.18	0.22	0.19	0.20	0.36	0.33	0.28	0.31
	Mean	0.25	0.27	0.30	0.35	0.18	0.16	0.13	0.14	0.16	0.17	0.18	0.21	0.15	0.17	0.15	0.15	0.21	0.23	0.20	0.22
	Min	0.21	0.23	0.23	0.29	0.13	0.11	0.10	0.12	0.12	0.14	0.15	0.17	0.12	0.14	0.13	0.12	0.13	0.17	0.15	0.17
Cold	SD	0.05	0.04	0.07	0.10	0.08	0.08	0.05	0.05	0.08	0.06	0.05	0.04	0.05	0.06	0.04	0.04	0.16	0.13	0.07	0.10

Table 6 (continued)

Parts	CuBe$_2$NiTi bronze 0.5 mm + CuBe$_2$NiTi bronze 0.5 mm				CuZn37 brass 0.2 mm + CuZn37 brass 0.2 mm				CuZn37 brass 0.2 mm + CuZn37 brass 0.4 mm				CuZn37 brass 0.4 mm + CuZn37 brass 0.4 mm				CuZn37 brass 0.4 mm + Copper 0.8 mm			
Calculated mean bulk resistance at 20 °C, 10^{-10} Ω	0.90				0.28				0.42				0.56				0.42			
Current modes	1	2	3	4	1	2	3	4	1	2	3	4	1	2	3	4	1	2	3	4
MAD	0.04	0.03	0.06	0.08	0.07	0.06	0.04	0.04	0.07	0.05	0.04	0.04	0.04	0.04	0.03	0.03	0.13	0.10	0.06	0.08
Preheated — SD	0.02	0.02	0.04	0.03	0.02	0.02	0.02	0.03	0.02	0.02	0.02	0.02	0.02	0.02	0.01	0.02	0.05	0.03	0.03	0.03
MAD	0.02	0.02	0.03	0.03	0.02	0.02	0.02	0.03	0.02	0.01	0.01	0.02	0.01	0.01	0.01	0.01	0.04	0.02	0.02	0.02

Parts	Stainless steel 0.3 mm + Stainless steel 0.3 mm				Stainless steel 0.3 mm + Stainless steel 0.5 mm				Stainless steel 0.3 mm + Stainless steel 0.8 mm				Stainless steel 0.5 mm + Stainless steel 0.5 mm				Stainless steel 0.8 mm + Stainless steel 0.8 mm			
Calculated mean bulk resistance at 20 °C, 10^{-10} Ω	4.38				5.84				8.03				7.30				11.68			
Current modes	1	2	3	4	1	2	3	4	1	2	3	4	1	2	3	4	1	2	3	4
RBE cold (mΩ) — Max	3.26	3.17	4.39	4.27	5.61	4.44	5.37	4.57	4.81	4.95	4.09	4.82	5.80	5.99	5.81	5.01	4.72	5.88	5.09	5.84
Mean	2.30	1.99	2.55	2.14	3.41	2.81	3.00	2.56	3.11	3.02	2.62	2.74	3.31	3.82	3.79	3.46	2.88	3.98	3.78	4.13
Min	0.85	1.08	1.35	1.31	1.77	1.65	1.50	1.47	1.72	2.13	1.85	1.65	2.14	1.91	2.24	2.34	1.83	2.45	2.72	2.63
RBE preheated (mΩ) — Max	1.13	1.19	1.12	1.19	1.39	1.45	1.36	1.39	1.41	1.46	1.56	1.50	1.47	1.55	1.53	1.54	1.51	1.61	1.73	1.75
Mean	1.00	1.04	1.00	1.04	1.26	1.27	1.22	1.24	1.27	1.27	1.38	1.29	1.34	1.42	1.40	1.42	1.37	1.48	1.53	1.55
Min	0.87	0.92	0.92	0.92	1.14	1.11	1.08	1.09	1.13	1.14	1.22	1.15	1.24	1.25	1.21	1.27	1.23	1.37	1.37	1.42
Cold — SD	0.38	0.41	0.61	0.54	0.73	0.59	0.72	0.49	0.63	0.50	0.37	0.51	0.68	0.62	0.82	0.47	0.49	0.62	0.43	0.63

Table 6 (continued)

Parts	Stainless steel 0.3 mm + Stainless steel 0.3 mm				Stainless steel 0.3 mm + Stainless steel 0.5 mm				Stainless steel 0.3 mm + Stainless steel 0.8 mm				Stainless steel 0.5 mm + Stainless steel 0.5 mm				Stainless steel 0.8 mm + Stainless steel 0.8 mm			
Calculated mean bulk resistance at 20 °C, 10^{-10} Ω	4.38				5.84				8.03				7.30				11.68			
Current modes	1	2	3	4	1	2	3	4	1	2	3	4	1	2	3	4	1	2	3	4
MAD	0.30	0.33	0.47	0.41	0.59	0.47	0.57	0.38	0.51	0.40	0.29	0.39	0.54	0.49	0.67	0.37	0.38	0.49	0.33	0.50
Preheated SD	0.05	0.04	0.04	0.05	0.04	0.06	0.05	0.05	0.05	0.06	0.05	0.07	0.04	0.05	0.05	0.04	0.05	0.04	0.05	0.05
MAD	0.04	0.03	0.03	0.04	0.03	0.05	0.04	0.04	0.04	0.05	0.04	0.05	0.03	0.04	0.04	0.04	0.04	0.04	0.04	0.04

| Parts	Ti–0.8Al–0.8Mn 0.5 mm + Ti–0.8Al–0.8Mn 0.5 mm				Ti–0.8Al–0.8Mn 0.5 mm + Zr–1Nb 0.5 mm				Zr–1Nb 0.5 mm + Zr–1Nb 0.5 mm				Zr–1Nb 0.5 mm + Zr–1Nb 0.8 mm				Zr–1Nb 0.8 mm + Zr–1Nb 0.8 mm			
Calculated mean bulk resistance at 20 °C, 10^{-10} Ω	4.20				4.95				5.70				7.41				9.12			
Current modes	1	2	3	4	1	2	3	4	1	2	3	4	1	2	3	4	1	2	3	4
RBE cold (mΩ) Max	3.09	4.73	5.98	5.30	3.14	3.94	5.26	5.78	5.66	5.89	3.63	4.82	3.97	5.38	5.38	4.57	3.42	4.63	5.18	4.26
Mean	2.21	3.22	4.49	2.79	2.04	3.02	3.76	4.04	3.69	3.60	2.34	3.06	2.62	3.40	3.86	3.16	2.06	2.66	2.96	2.87
Min	1.58	2.17	2.05	1.44	1.29	2.10	2.40	2.49	1.69	1.98	1.28	1.82	1.31	1.82	2.41	1.72	1.29	1.44	1.75	1.82
RBE preheated (mΩ) Max	1.98	1.97	2.02	1.73	1.50	1.50	1.70	1.68	1.45	1.45	1.30	1.38	1.42	1.42	1.60	1.48	1.38	1.45	1.62	1.41
Mean	1.82	1.79	1.88	1.54	1.27	1.40	1.56	1.51	1.36	1.34	1.16	1.29	1.24	1.26	1.43	1.29	1.21	1.21	1.35	1.26
Min	1.38	1.44	1.39	1.31	1.11	1.25	1.39	1.38	1.25	1.23	1.05	1.18	1.11	1.14	1.30	1.12	1.08	1.11	1.26	1.13
Cold SD	0.34	0.55	0.80	0.97	0.39	0.36	0.54	0.59	0.76	0.74	0.47	0.64	0.68	0.71	0.60	0.57	0.45	0.74	0.66	0.36
MAD	0.28	0.44	0.62	0.82	0.30	0.28	0.44	0.46	0.61	0.63	0.38	0.53	0.58	0.58	0.49	0.46	0.38	0.62	0.54	0.27
Preheated SD	0.10	0.11	0.11	0.10	0.09	0.05	0.05	0.05	0.04	0.04	0.04	0.04	0.06	0.06	0.05	0.09	0.06	0.05	0.05	0.06
MAD	0.08	0.09	0.08	0.09	0.07	0.04	0.04	0.04	0.04	0.03	0.04	0.04	0.05	0.05	0.04	0.08	0.05	0.04	0.04	0.04
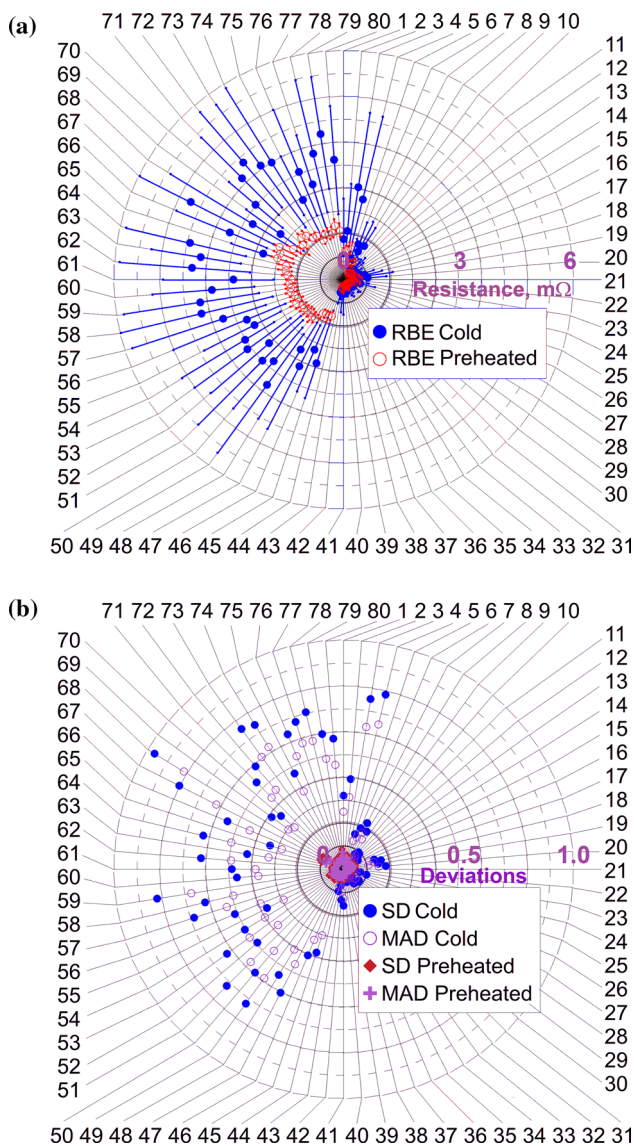
Fig. 4 Radar diagrams: **a** mean RBE values and their dispersions; **b** RBE deviations (the numerical data and the legend to the numbered axes are presented in Tables 6 and 7, respectively)

in the preheated RBE values ranged from − 0.80 up to 0.64, and the generalized ones for all studied materials were about zero (Table 10).

Discussion

The discussion of the obtained results had to be started with the fact that the dispersions of the preheated RBE values were rather high, considering their effect on heat input in RSW by linear dependence according to formula (1) and, respectively, on the quality of welded joints. In addition, these studies were performed using the carefully prepared surfaces under laboratory conditions. In industrial mass production, similar

results were expected to be much worse, since it is known (Holm, 1981; Merl, 1962; Usov, 1963) that contact resistances of pure rough metal surfaces were determined mainly by the tunneling effect due to current constriction at contacted microroughnesses. In this case, electrons could (with some degree of probability) penetrate through a thin barrier layer (a potential one) if their own wavelength was commensurate with thicknesses of the surface films. On real metal surfaces, the total contact resistances could not be calculated by adding the contact resistance of a pure metal contact to resistances of oxides, sulfides and other contaminants, since the surface film changed the current density distribution near the contact surface. It was more uniform and, accordingly, the contact resistance was higher. In general cases, current flowed through several contact spots, unevenly distributed over a common contact surface area. The thicker the oxide films were, the smaller the contribution to the contact resistance was made by the tunneling effect.

It was also necessary to consider in more detail the current possibilities of modeling real contact surfaces and theoretical calculation of cold RBE values with any acceptable degree of confidence. Analysis of the data published in the reference books by Merl (1962); Usov (1963); Samsonov (1973); and Lazarev el al. (1983), which were summarized in Table 5, enabled to conclude that the solution of such problems is impossible for most (may be all) contact pairs of real metal surfaces. This statement was based on the following reasons.

Firstly, the nature of conductivity of various possible oxides on the studied materials was different. They could be dielectrics (Al_2O_3, Cr_2O_3, MnO, NiO, TiO_2, and ZrO_2), semiconductors of both *n*- and *p*-types (CrO_3, CuO_2, FeO, Fe_3O_4, Fe_2O_3, Mn_3O_4, Mn_2O_3, and NbO_2), or be characterized by metallic conductivity (CrO_2 and Nb_2O_5). In addition, conductivity of some oxides (if they were actually present on the surfaces) could change depending on temperature. For example, Ti_2O_3 could be a semiconductor–metal (or semimetal) due to the uncertainty of the criteria and the discrepancy in the properties of the high-temperature phase (Lazarev el al., 1983).

Secondly, it was impossible to predict chemical compositions of the surface layers even in the laboratory conditions, when they were mainly covered with oxides only (highly likely, there were no significant amounts of sulfides, oxy(carbo)nitrides and other chemical compounds after careful preparation of the parts). This fact was due to the different physical and chemical properties of the studied materials. For instance, copper, as an ideal conductor, was characterized by the highest values of both electrical and thermal conductivity. All alloying elements in brass and bronze reduced electrical conductivity (the degree of change was determined by the nature of their interaction with copper). If the elements had not formed solid solutions with copper, then the

Table 7 The legend of the numbered radar chart axes in Fig. 4

No	Parts	Mode	No	Parts	Mode	No	Parts	Mode	No	Parts	Mode
1	Al–6Mg 1.0 mm + Al–6Mg 1.0 mm	1	21	CuBe2NiTi bronze 0.5 mm + CuBe2NiTi bronze 0.5 mm	1	41	Stainless steel 0.3 mm + Stainless steel 0.3 mm	1	61	Ti–0.8Al–0.8Mn 0.5 mm + Ti–0.8Al–0.8Mn 0.5 mm	1
2	Al–6Mg 1.0 mm + Al–6Mg 1.0 mm	2	22	CuBe2NiTi bronze 0.5 mm + CuBe2NiTi bronze 0.5 mm	2	42	Stainless steel 0.3 mm + Stainless steel 0.3 mm	2	62	Ti–0.8Al–0.8Mn 0.5 mm + Ti–0.8Al–0.8Mn 0.5 mm	2
3	Al–6Mg 1.0 mm + Al–6Mg 1.0 mm	3	23	CuBe2NiTi bronze 0.5 mm + CuBe2NiTi bronze 0.5 mm	3	43	Stainless steel 0.3 mm + Stainless steel 0.3 mm	3	63	Ti–0.8Al–0.8Mn 0.5 mm + Ti–0.8Al–0.8Mn 0.5 mm	3
4	Al–6Mg 1.0 mm + Al–6 Mg 1.0 mm	4	24	CuBe2NiTi bronze 0.5 mm + CuBe2NiTi bronze 0.5 mm	4	44	Stainless steel 0.3 mm + Stainless steel 0.3 mm	4	64	Ti–0.8Al–0.8Mn 0.5 mm + Ti–0.8Al–0.8Mn 0.5 mm	4
5	Al-6 Mg 1.0 mm + Copper 0.8 mm	1	25	CuZn37 brass 0.2 mm + CuZn37 brass 0.2 mm	1	45	Stainless steel 0.3 mm + Stainless steel 0.5 mm	1	65	Ti-0.8Al-0.8Mn 0.5 mm + Zr-1Nb 0.5 mm	1
6	Al–6Mg 1.0 mm + Copper 0.8 mm	2	26	CuZn37 brass 0.2 mm + CuZn37 brass 0.2 mm	2	46	Stainless steel 0.3 mm + Stainless steel 0.5 mm	2	66	Ti–0.8Al–0.8Mn 0.5 mm + Zr–1Nb 0.5 mm	2
7	Al-6 Mg 1.0 mm + Copper 0.8 mm	3	27	CuZn37 brass 0.2 mm + CuZn37 brass 0.2 mm	3	47	Stainless steel 0.3 mm + Stainless steel 0.5 mm	3	67	Ti-0.8Al-0.8Mn 0.5 mm + Zr-1Nb 0.5 mm	3
8	Al–6Mg 1.0 mm + Copper 0.8 mm	4	28	CuZn37 brass 0.2 mm + CuZn37 brass 0.2 mm	4	48	Stainless steel 0.3 mm + Stainless steel 0.5 mm	4	68	Ti–0.8Al–0.8Mn 0.5 mm + Zr–1Nb 0.5 mm	4
9	Copper 0.8 mm + Copper 0.8 mm	1	29	CuZn37 brass 0.2 mm + CuZn37 brass 0.4 mm	1	49	Stainless steel 0.3 mm + Stainless steel 0.8 mm	1	69	Zr–1Nb 0.5 mm + Zr–1Nb 0.5 mm	1

Table 7 (continued)

No	Parts	Mode	No	Parts	Mode	No	Parts	Mode	No	Parts	Mode
10	Copper 0.8 mm + Copper 0.8 mm	2	30	CuZn37 brass 0.2 mm + CuZn37 brass 0.4 mm	2	50	Stainless steel 0.3 mm + Stainless steel 0.8 mm	2	70	Zr–1Nb 0.5 mm + Zr–1Nb 0.5 mm	2
11	Copper 0.8 mm + Copper 0.8 mm	3	31	CuZn37 brass 0.2 mm + CuZn37 brass 0.4 mm	3	51	Stainless steel 0.3 mm + Stainless steel 0.8 mm	3	71	Zr–1Nb 0.5 mm + Zr–1Nb 0.5 mm	3
12	Copper 0.8 mm + Copper 0.8 mm	4	32	CuZn37 brass 0.2 mm + CuZn37 brass 0.4 mm	4	52	Stainless steel 0.3 mm + Stainless steel 0.8 mm	4	72	Zr-1Nb 0.5 mm + Zr-1Nb 0.5 mm	4
13	CuBe$_2$NiTi bronze 0.2 mm + CuBe$_2$NiTi bronze 0.2 mm	1	33	CuZn37 brass 0.4 mm + CuZn37 brass 0.4 mm	1	53	Stainless steel 0.5 mm + Stainless steel 0.5 mm	1	73	Zr–1Nb 0.5 mm + Zr–1Nb 0.8 mm	1
14	CuBe$_2$NiTi bronze 0.2 mm + CuBe$_2$NiTi bronze 0.2 mm	2	34	CuZn37 brass 0.4 mm + CuZn37 brass 0.4 mm	2	54	Stainless steel 0.5 mm + Stainless steel 0.5 mm	2	74	Zr–1Nb 0.5 mm + Zr–1Nb 0.8 mm	2
15	CuBe$_2$NiTi bronze 0.2 mm + CuBe$_2$NiTi bronze 0.2 mm	3	35	CuZn37 brass 0.4 mm + CuZn37 brass 0.4 mm	3	55	Stainless steel 0.5 mm + Stainless steel 0.5 mm	3	75	Zr–1Nb 0.5 mm + Zr–1Nb 0.8 mm	3
16	CuBe$_2$NiTi bronze 0.2 mm + CuBe$_2$NiTi bronze 0.2 mm	4	36	CuZn37 brass 0.4 mm + CuZn37 brass 0.4 mm	4	56	Stainless steel 0.5 mm + Stainless steel 0.5 mm	4	76	Zr–1Nb 0.5 mm + Zr–1Nb 0.8 mm	4
17	CuBe$_2$NiTi bronze 0.2 mm + CuBe$_2$NiTi bronze 0.5 mm	1	37	CuZn37 brass 0.4 mm + Copper 0.8 mm	1	57	Stainless steel 0.8 mm + Stainless steel 0.8 mm	1	77	Zr–1Nb 0.8 mm + Zr–1Nb 0.8 mm	1
18	CuBe$_2$NiTi bronze 0.2 mm + CuBe$_2$NiTi bronze 0.5 mm	2	38	CuZn37 brass 0.4 mm + Copper 0.8 mm	2	58	Stainless steel 0.8 mm + Stainless steel 0.8 mm	2	78	Zr–1Nb 0.8 mm + Zr–1Nb 0.8 mm	2

Table 7 (continued)

No	Parts	Mode	No	Parts	Mode	No	Parts	Mode	No	Parts	Mode
19	CuBe$_2$NiTi bronze 0.2 mm + CuBe$_2$NiTi bronze 0.5 mm	3	39	CuZn37 brass 0.4 mm + Copper 0.8 mm	3	59	Stainless steel 0.8 mm + Stainless steel 0.8 mm	3	79	Zr–1Nb 0.8 mm + Zr–1Nb 0.8 mm	3
20	CuBe$_2$NiTi bronze 0.2 mm + CuBe$_2$NiTi bronze 0.5 mm	4	40	CuZn37 brass 0.4 mm + Copper 0.8 mm	4	60	Stainless steel 0.8 mm + Stainless steel 0.8 mm	4	80	Zr–1Nb 0.8 mm + Zr–1Nb 0.8 mm	4

Table 8 The correlation coefficients between the calculated mean bulk resistance values at 20 °C and the experimentally determined RBE ones, as well as their deviations

Maximum cold RBE	0.86
Mean cold RBE	0.87
Minimum cold RBE	0.89
Maximum preheated RBE	0.86
Mean preheated RBE	0.86
Minimum preheated RBE	0.88
Cold SD	0.74
Cold MAD	0.73
Preheated SD	0.46
Preheated MAD	0.45

effect depended on the distribution of particles, their concentration and electrical conductivity. If alloying elements had been dissolved in copper, then electrical conductivity was determined only by their concentration in the solid solution. Most probably, oxygen was present in the surface layer of the investigated parts as the Cu$_2$O compound, which formed the Cu$_2$O–Cu eutectic with copper. At room temperature, the typical thickness of the oxide layers was about 50 nm. The solubility of oxygen in solid copper was low and its limiting concentration was only 0.008% at a eutectic temperature of 1066 °C. It should be noted the the Cu$_2$O compound had a negative effect on plasticity of the surface layers as well. In addition, the characteristic feature of the oxygen-enriched surface zones was smaller grain sizes compared to those in the base metal. In real production conditions, layers of several oxides (CuO on the outer surface and Cu$_2$O in the zone of contact with the metal) could be on the surface of copper and its alloys (Holm, 1981; Lazarev el al., 1983; Osintsev and Fedorov, 2004). The aluminum alloy parts were another example. A continuous oxide film with a thickness of at least

2.5–3.0 nm was unambiguously on their surfaces. The molecular volume of such films is almost 1.3 times greater than the volume of aluminum participated in the oxidation reaction. Therefore, the surface layer was under compressive stresses and quickly recovered if it was damaged (Hatch, 1984). There was a high probability that ceramic ZrO$_2$ films were on the surfaces of the Zr–1Nb alloy parts, but not necessarily of the stoichiometric composition. However, it was also possible that niobium was present in the form of Nb$_2$O$_5$ or 6ZrO$_2$·Nb$_2$O$_5$. It could locate along the boundaries of ZrO$_2$ crystallites and contributed to self-healing of discontinuities (Zaimovsky et al., 1981). According to Holm (1981), surface films were relatively thin (from 1 up to 2 nm) on the (Grade 321) stainless steel, so it was permeable to tunneling electrons. However, its composition cannot be unambiguously predicted considering the number of the alloying elements.

Thirdly, the specific electrical resistance values of the oxides published in various reference books differed by several orders of magnitude in some cases (Table 5). In addition, any data on some ones possibly presented on the surfaces of the studied materials were not found at all. Also, resistivity of the oxides could change quite significantly with minimal deviations of their composition from the stoichiometric values. For example, the conductivity of Cu$_2$O was in the range of 10^{10}–10^{12} Ω m, but it was ~ 10^8 Ω m for CuO, ~ 10^5 Ω m for Cu$_2$O–Cu, and ~ 1.724×10^{-8} Ω m for pure copper at room temperature (the data were taken from (Merl, 1962; Osintsev & Fedorov, 2004; Usov, 1963), but they differed in other reference books (Lazarev et al., 1983; Samsonov, 1973) according to Table 5). Respectively, a deviation of 10^{-3} Ω m could cause an increase in conductivity by three orders of magnitude. This phenomenon was explained by Merl (1962) using a rigid body model with different energy levels. The studied contacts of the real metals were, in principle, insulators. Charge carriers, required for electrical conductivity, were gradually released as the temperature increased or moved from the outside with foreign

Table 9 The ratios of the maximum and minimum RBE values grouped by materials

Resistance		Aluminium alloy	Aluminium alloy and coper	Copper and its alloys	Stainless steel	Titanium and zirconium alloys
RBE cold (mΩ)	Max	4.43	1.70	1.30	5.99	5.98
	Min	0.62	0.31	0.12	0.85	1.28
	Max/Min	7.17	5.41	11.06	7.03	4.68
RBE preheated (mΩ)	Max	1.01	0.64	0.49	1.75	2.02
	Min	0.62	0.28	0.10	0.87	1.05
	Max/Min	1.64	2.28	4.85	2.00	1.92

Table 10 The correlation coefficients between the deviations of the preheated RBE values and the current modes grouped by similar materials

Correlation coefficients	Aluminium alloy	Aluminium alloy and coper	Copper and its alloys	Stainless steel	Titanium and zirconium alloys	Generalized
SD	0.62	− 0.80	− 0.01	0.24	− 0.02	− 0.02
MAD	0.64	− 0.78	− 0.01	0.21	− 0.02	− 0.02

atoms. Both electrons and holes in the filled energy level of electrons could be charge carriers (they behaved like positive electrons in this case). Conductivity of semiconductor films was very low compared to that of the metals (it reached levels six orders of magnitude lower in some cases). This residual conductivity played an important role in the breakdown of the surface films (at sufficiently thick films and high voltages) and upon fritting (in other cases), although contact fritting was limited by electrical strength of thicker, poorly conducted surface films.

Last but not least, the dynamics of the RSW processes could be different after squeezing the parts with electrodes. This depended on the variation in the mechanical properties of rolled metal from different delivery batches, metal contamination, thermomechanical processing routs, etc. It is known that the highest microroughnesses of all metal surfaces covered with oxide films were in contact initially. Then, these microroughnesses were elastically deformed, contact surface areas were greatly enlarged, and the surface films were fractured. At the same time, new contact spots arose between lower microroughnesses. As a result, individual contact spots were combined into large areas. In the contacts, the deformation processes were very complicated, because the plasticized materials not only moved to the sides, but also into the depth. In this case, work hardening of the metal surface layers and distortion of their crystal lattices occurred (Holm, 1981; Merl, 1962; Usov, 1963). However, the mechanical properties of the studied materials could also differ significantly depending on the previous production route, chemical and phase compositions, and preliminary heat treatment (Zaimovsky et al., 1981; Collings,

1984; Hatch, 1984; Osintsev & Fedorov, 2004; IAEA, 2008). Current flows heated the contacts, and the above processes were intensified many times. In addition, the materials dilatometrically expanded (which further increased stresses) and their temperature-depended physical properties changed as well. As a result, the RBE values typically reduced (not in all cases as mentioned above), since the overall decrease in contact resistance significantly exceeded lowering electrical conductivity of the materials with rising temperature (Paton & Lebedev, 1969). However, the dynamic resistances were determined by the thicknesses and properties of the oxide films, since they differed not only in electrical conductivity, but also, among other things, in their mechanical characteristics. Some ones were hard and brittle; others could be soft and flowing. Accordingly, brittle films cracked and delaminated. At the same time, solid but thin ones that weakly adhered to the metals, had little effect on the RBE values. Loose films could cause a sharp change in the RBE levels, but plastic ones could be pressed into gaps between the contacted microroughnesses, filled them and enhanced the contact resistances (Merl, 1962; Usov, 1963). As a result, such a large number of uncertainties did not enable to reveal any generalized patterns of the RBE value stabilization depending on the algorithm for energy input through the applied preheating current pulses for the studied materials.

The presented experimental results in connection with the theoretical background are another step in the development feedback-based approach for improving RSW procedures implemented in production routs within the intelligent manufacturing framework (Zhong et al., 2017) of the Industry

4.0 concept (Lasi et al., 2014; Lee et al., 2015). In particular, it could be recommended that further directions of research should be the development both RSW equipment controlled with digital signal processors, as well as welding procedures based on adaptive change in welding current (and, accordingly, heat input) depending on the RBE values after preheating. In real time, the data should be obtained by feedback, filtered from noise and recognized using artificial intelligence algorithms (neural networks, fuzzy logic, etc.). Welding current profiles should be preset considering materials and thicknesses of the parts to be welded. In this case, not only their amplitude and duration should be considered for the formation of weld nuggets with required dimensions, but preheating parts should also enable to measure current and voltage, process these data and decide which welding current profile is the most suitable. Also, final smooth welding current reduction seems to be useful for reducing the formation of quenching microstructures and residual stresses. All the suggested activities might improve future correlations of 'digital twins' of RSW joints with their real-world counterparts, which greatly determine the integrity of numerous critical structures.

Conclusions

The obtained results, aimed at improving the feedback-based approach for controlling RSW procedures implemented in production routs within the intelligent manufacturing framework (Zhong et al., 2017) of the Industry 4.0 concept (Lasi et al., 2014; Lee et al., 2015), enabled to draw the following conclusions.

After reaching the first goal, namely deeper understanding the effect of the preheating current diagrams on the stabilization of RBE values and, accordingly, heat input in RSW, the following theses were stated. All studied preheating pulses had a positive effect on the RBE stabilization. After current flowing, the range of the dispersions between the maximum and minimum RBE values significantly decreased from about 5–11 down to 2–5 times. However, the influence of the investigated algorithms of the preheating current pulses on the RBE stabilization was not observed. The correlation coefficients between the used current modes and the variations in the preheated RBE values ranged from -0.80 up to 0.64, and the generalized ones for all studied materials were about zero.

When the second goal was achieved, which had been to assess the possibilities to reliably evaluate and control of heat input in the RSW process of different materials by measuring indirect parameters, namely current and voltage, followed by statistical processing of these data, the authors were able to formulate the following statements:

- The distortion of the experimentally measured dynamic resistance curves increased with raising the specific electrical resistance of the parts.
- In general, there was a correspondence of the minimum, mean and maximum RBE values (both cold and preheated) to specific electrical resistances of the parts at room temperature, the level of which was approximately four orders of magnitude lower. The correlation coefficients between these parameters were from 0.86 to 0.89, but the ones between the specific electrical resistances of the parts and the variance of the cold RBE values were significantly lower (0.74 for SD and 0.73 for MAD). The specific electrical resistance levels of the parts did not affect the variance of the preheated RBE values at all (the correlation coefficients were only 0.46 and 0.45 for SD and MAD, respectively).
- The 'standard deviation' statistical function was better suited for processing the RBE values of than the 'mean absolute deviation' one.

Based on these findings, the authors proposed the following future research directions. For improving the feedback-based approach for controlling RSW procedures implemented in production routs within the intelligent manufacturing framework (Zhong et al., 2017) of the Industry 4.0 concept (Lasi et al., 2014; Lee et al., 2015), there is a need for the development both RSW equipment controlled with digital signal processors, as well as welding procedures based on adaptive change in welding current (and, accordingly, heat input) depending on the RBE values after preheating. In real time, the data should be obtained by feedback, filtered from noise and recognized using artificial intelligence algorithms (neural networks, fuzzy logic, etc.). Welding current profiles should be preset considering materials and thicknesses of the parts to be welded. In this case, not only their amplitude and duration should be considered for the formation of weld nuggets with required dimensions, but preheating parts should also enable to measure current and voltage, process these data and decide which welding current profile is the most suitable. Also, final smooth welding current reduction seems to be useful for reducing the formation of quenching microstructures and residual stresses. As a result, future correlations of 'digital twins' of RSW joints with their real-world counterparts, which greatly determine the integrity of numerous critical structures, might be improved to a certain degree.

Declarations

References

Ahmed, F., Jannat, N.-E., Schmidt, D., & Kim, K.-Y. (2021). Data-driven cyber-physical system framework for connected resistance spot welding weldability certification. *Robotics and Computer-Integrated Manufacturing, 67*, 102036. https://doi.org/10.1016/j.rcim.2020.102036

Akbolatov, E. Z., Kiselev, A. S., & Slobodyan, M. S. (2019). Prediction and stabilization of initial resistance between electrodes for small-scale resistance spot welding. *Welding in the World, 63*(2), 443–457. https://doi.org/10.1007/s40194-018-0671-x

Aufiqurrahman, I., Ahmad, A., Mustapha, M., Ginta, T. L., Haryoko, L. A. F., & Shozib, I. A. (2021). The effect of welding current and electrode force on the heat input, weld diameter, and physical and mechanical properties of SS316l/Ti6Al4V dissimilar resistance spot welding with aluminum interlayer. *Materials, 14*(5), 1129. https://doi.org/10.3390/ma14051129

Batista, M., Furlanetto, V., & Brandi, S. D. (2020). Analysis of the behavior of dynamic resistance, electrical energy and force between the electrodes in resistance spot welding using additive manufacturing. *Metals, 10*(5), 690. https://doi.org/10.3390/met10050690

Brechelt, S., Wiche, H., & Wesling, V. (2019). Influence of pre-pulse in spot weld bonding of three-sheet steel stack-up. *Welding in the World, 63*, 771–782. https://doi.org/10.1007/s40194-019-00706-3

Collings, E.W. (1984). *The Physical Metallurgy of Titanium Alloys*. American Society for Metals.

Dai, W., Li, D., Tang, D., Jiang, Q., Wang, D., Wang, H., & Peng, Y. (2021). Deep learning assisted vision inspection of resistance spot welds. *Journal of Manufacturing Processes, 62*, 262–274. https://doi.org/10.1016/j.jmapro.2020.12.015

Dejans, A., Kurtov, O., & Van Rymenant, P. (2021). Acoustic emission as a tool for prediction of nugget diameter in resistance spot welding. *Journal of Manufacturing Processes, 62*, 7–17. https://doi.org/10.1016/j.jmapro.2020.12.002

Ghafarallahi, E., Farrahi, G. H., & Amiri, N. (2021). Acoustic simulation of ultrasonic testing and neural network used for diameter prediction of three-sheet spot welded joints. *Journal of Manufacturing Processes, 64*, 1507–1516. https://doi.org/10.1016/j.jmapro.2021.03.012

Gnyusov, S. F., Kiselev, A. S., Slobodyan, M. S., Sovetchenko, B. F., Nekhoda, M. M., Srukov, A. V., & Yurin, P. M. (2005). Formation of a joint in resistance spot microwelding. *Welding International, 19*(9), 737–741. https://doi.org/10.1533/wint.2005.3510

GOST 15527-2004 Wrought copper-zinc alloys (brass). Grades (Russian State Standard, in Russian)

GOST 18175-78 Wrought tinless bronze. Grades (Russian State Standard, in Russian)

GOST 19807-91 Titanium and wrought titanium alloys. Grades (Russian State Standard, in Russian)

GOST 4784-97 Aluminum and wrought aluminum alloys (Russian State Standard, in Russian)

GOST 58175-2014 Stainless steels and corrosion resisting, heat-resisting and creep resisting alloys. Grades (Russian State Standard, in Russian)

GOST 859-2001 Copper. Grades (Russian State Standard, in Russian)

Hatch, J.E. (1984). *Aluminum: Properties and physical metallurgy*. ASM International.

Hernández, A. E., Villarinho, L. O., Ferraresi, V. A., Orozco, M. S., Roca, A. S., & Fals, H. C. (2020). Optimization of resistance spot welding process parameters of dissimilar DP600/AISI304 joints using the infrared thermal image processing. *International Journal of Advanced Manufacturing Technology, 108*(1–2), 211–221. https://doi.org/10.1007/s00170-020-05374-y

Holm, R. (1981). *Electric contacts. Theory and application* (4th Edn.). Springer-Verlag. https://doi.org/10.1007/978-3-662-06688-1

Ji, C., Na, J. K., Lee, Y.-S., Park, Y.-D., & Kimchi, M. (2021). Robot-assisted non-destructive testing of automotive resistance spot welds. *Welding in the World, 65*(1), 119–126. https://doi.org/10.1007/s40194-020-01002-1

Kiselev, A. S., & Slobodyan, M. S. (2019). Effects of electrode degradation on properties of small-scale resistance spot welded joints of E110 alloy. *Materials Science Forum, 970*, 227–235. https://doi.org/10.4028/www.scientific.net/MSF.970.227

Klimenov, V., Slobodyan, M., Ivanov, Y., Kiselev, A., & Matrenin, S. (2020). Metallurgy of a Ti–Au alloy synthesized by controlled electric resistance fusion. *Intermetallics, 127*, 06968. https://doi.org/10.1016/j.intermet.2020.106968

Lasi, H., Fettke, P., Kemper, H.-G., Feld, T., & Hoffmann, M. (2014). Industry 4.0. *Business and Information Systems Engineering, 6*, 239–242. https://doi.org/10.1007/s12599-014-0334-4

Lazarev, V. B., Sobolev, V. V., & Shaplygin, I. S. (1983). *Chemical and physical properties of simple metal oxides*. Science. (in Russian)

Lee, H.-T., & Chang, Y.-C. (2020). Effect of double pulse resistance spot welding process on 15B22 hot stamped boron steel. *Metals, 10*, 1279. https://doi.org/10.3390/met10101279

Lee, J., Bagheri, B., & Kao, H.-A. (2015). A cyber-physical systems architecture for Industry 4.0-based manufacturing systems. *Manufacturing Letters, 3*, 18–23. https://doi.org/10.1016/j.mfglet.2014.12.001

Li, B.-H., Hou, B.-C., Yu, W.-T., Lu, X.-B., & Yang, C.-W. (2017). Applications of artificial intelligence in intelligent manufacturing: A review. *Frontiers of Information Technology and Electronic Engineering, 18*, 86–96. https://doi.org/10.1631/FITEE.1601885

Liu, X., & Wei, Y. (2020). Direct finite element analysis of the stress evolution and interaction in resistance spot welding with multiple processes and multiple spots based on reverse engineering technology. *Journal of Materials Engineering and Performance, 29*(8), 5490–5502. https://doi.org/10.1007/s11665-020-04997-2

Merl, W. (1962). *Electrical contact*. Gosenergoizdat. (in Russian).

Online document IAEA. (2008). *Thermophysical properties of materials for nuclear engineering: A tutorial and collection of data*. Retrieved June 30, 2022, from https://www-pub.iaea.org/MTCD/Publications/PDF/IAEA-THPH_web.pdf

Orlov, B. D. (1975). *Technology and equipment for resistance welding*. Mechanical Engineering. (In Russian)

Osintsev, O. E., & Fedorov, V. N. (2004). *Copper and copper alloys. domestic and foreign grades: Reference Book*. Mechanical Engineering. (in Russian)

Pashazadeh, H., Gheisari, Y., & Hamedi, M. (2016). Statistical modeling and optimization of resistance spot welding process parameters using neural networks and multi-objective genetic algorithm. *Journal of Intelligent Manufacturing, 27*, 549–559. https://doi.org/10.1007/s10845-014-0891-x

Paton, B. E., & Lebedev, V. K. (1969). *Electrical equipment for resistance welding. elements of the theory*. Mechanical Engineering. (in Russian)

Piott, M., Werber, A., Schleuss, L., Doynov, N., Ossenbrink, R., & Michailov, V. G. (2020). A study of the heat transfer mechanism in resistance spot welding of aluminum alloys AA5182 and AA6014. *International Journal of Advanced Manufacturing Technology, 111*(1–2), 263–271. https://doi.org/10.1007/s00170-020-05650-x

Şahin, S., Hayat, F., & Çölgeçen, O. C. (2021). The effect of welding current on nugget geometry, microstructure and mechanical properties of TWIP steels in resistance spot welding. *Welding in the World, 65*, 921–935. https://doi.org/10.1007/s40194-021-01083-6

Samsonov, G. V. (1973). *The oxide handbook*. IFI/PLENUM.

Slobodyan, M. S., & Kiselev, A. S. (2019). Optimization of welding parameters for small-scale resistance spot welding of zirconium

alloys. *Materials Science Forum, 970*, 145–152. https://doi.org/10.4028/www.scientific.net/MSF.970.145

Smith, M. J. (2018). *Statistical analysis handbook*. The Winchelsea Press.

Sokolov, N. M. (1971). *Microwelding in mass production of radio valves*. Privolzhsky Publishing House. (In Russian)

Soomro, I. A., Pedapati, S. R., & Awang, M. (2021). Optimization of postweld tempering pulse parameters for maximum load bearing and failure energy absorption in dual phase (DP590) steel resistance spot welds. *Materials Science and Engineering A, 803*, 140713. https://doi.org/10.1016/j.msea.2020.140713

Stadler, M., Schnitzer, R., Gruber, M., Steineder, K., & Hofer, C. (2021). Influence of the cooling time on the microstructural evolution and mechanical performance of a double pulse resistance spot welded medium-Mn steel. *Metals, 11*(2), 270. https://doi.org/10.3390/met11020270

Tercan, H., & Meisen, T. (2022). Machine learning and deep learning based predictive quality in manufacturing: A systematic review. *Journal of Intelligent Manufacturing*. https://doi.org/10.1007/s10845-022-01963-8

TU 95.166-98 Zirconium alloys in ingots. Russian technical specification (in Russian)

Usov, V. V. (1963). *Metallurgy of electrical contacts*. Gosenergoizdat (in Russian)

Wang, X., Zhou, K., & Shen, S. (2021). Intelligent parameters measurement of electrical structure of medium frequency DC resistance spot welding system. *Measurement, 171*, 108795. https://doi.org/10.1016/j.measurement.2020.108795

Wang, Y., Rao, Z., & Wang, F. (2020). Heat evolution and nugget formation of resistance spot welding under multi-pulsed current waveforms. *International Journal of Advanced Manufacturing Technology, 111*(11–12), 3583–3595. https://doi.org/10.1007/s00170-020-06337-z

Wohner, M., Mitzschke, N., & Jüttner, S. (2021). Resistance spot welding with variable electrode force –development and benefit of a force profile to extend the weldability of 22MnB5+AS150. *Welding in the World, 65*(1), 105–117. https://doi.org/10.1007/s40194-020-01001-2

Xia, Y.-J., Su, Z.-W., Lou, M., Li, Y.-B., & Carlson, B. E. (2020). Online precision measurement of weld indentation in resistance spot welding using servo gun. *IEEE Transactions on Instrumentation and Measurement, 69*(7), 4465–4475. https://doi.org/10.1109/TIM.2019.2943981

Xia, Y.-J., Zhou, L., Shen, Y., Wegner, D.M., Haselhuhn, A.S., Li, Y.-B., & Carlson, B.E. (2021). Online measurement of weld penetration in robotic resistance spot welding using electrode displacement signals. *Measurement*, *168*, 108397. https://doi.org/10.1016/j.measurement.2020.108397

Xiao, M., Yang, B., Wang, S., Chang, Y., Li, S., & Yi, G. (2022). Research on recognition methods of spot-welding surface appearances based on transfer learning and a lightweight high-precision convolutional neural network. *Journal of Intelligent Manufacturing*. https://doi.org/10.1007/s10845-022-01909-0

Younes, D., Alghannam, E., Tan, Y., & Lu, H. (2020). Enhancement in quality estimation of resistance spot welding using vision system and fuzzy support vector machine. *Symmetry, 12*(8), 1380. https://doi.org/10.3390/sym12081380

Zaimovsky, A.S., Nikulina, A.V., & Reshetnikov, N.G. (1981). *Zirconium alloys in the nuclear industry*. Energoizdat (in Russian)

Zeng, J., Cao, B., & Tian, R. (2020). Quality monitoring for micro resistance spot welding with class-imbalanced data based on anomaly detection. *Applied Sciences, 10*(12), 4204. https://doi.org/10.3390/app10124204

Zhang, Q., Huang, M., Lv, T., Lou, M., & Li, Y. (2020a). Effect of surface treatments and storage conditions on resistance spot weldability of aluminum alloy 5182. *Journal of Manufacturing Processes, 58*, 30–40. https://doi.org/10.1016/j.jmapro.2020.08.002

Zhang, Y., Fu, C., Yi, R., & Ju, J. (2020b). Optimization of double-pulse process in resistance spot welding of hot stamped steel sheet. *ISIJ International, 60*(6), 1284–1290. https://doi.org/10.2355/isijinternational.ISIJINT-2019-579

Zhao, B., Wang, Y., Ding, K., Wu, G., Wei, T., Pan, H., & Gao, Y. (2021a). Enhanced cross-tension property of the resistance spot welded medium-Mn steel by in situ microstructure tailoring. *International Journal of Steel Structures, 21*, 666–675. https://doi.org/10.1007/s13296-021-00464-3

Zhao, D., Bezgans, Y., Wang, Y., Du, W., & Vdonin, N. (2021b). Research on the correlation between dynamic resistance and quality estimation of resistance spot welding. *Measurement: Journal of the International Measurement Confederation*, *168*, 108299. https://doi.org/10.1016/j.measurement.2020.108299

Zhao, D., Ivanov, M., Wang, Y., Liang, D., & Du, W. (2021c). Multi-objective optimization of the resistance spot welding process using a hybrid approach. *Journal of Intelligent Manufacturing, 32*, 2219–2234. https://doi.org/10.1007/s10845-020-01638-2

Zhong, R. Y., Xu, X., Klotz, E., & Newman, S. T. (2017). Intelligent manufacturing in the context of Industry 4.0: A review. *Engineering, 3*(5), 616–630. https://doi.org/10.1016/J.ENG.2017.05.015

Zhou, B., Pychynski, T., Reischl, M., Kharlamov, E., & Mikut, R. (2022a). Machine learning with domain knowledge for predictive quality monitoring in resistance spot welding. *Journal of Intelligent Manufacturing, 33*, 1139–1163. https://doi.org/10.1007/s10845-021-01892-y

Zhou, K., & Yao, P. (2019). Overview of recent advances of process analysis and quality control in resistance spot welding. *Mechanical Systems and Signal Processing, 124*, 170–198. https://doi.org/10.1016/j.ymssp.2019.01.041

Zhou, L., Li, T., Zheng, W., Zhang, Z., Lei, Z., Wu, L., Zhu, S., & Wang, W. (2022b). Online monitoring of resistance spot welding electrode wear state based on dynamic resistance. *Journal of Intelligent Manufacturing, 33*, 91–101. https://doi.org/10.1007/s10845-020-01650-6

Zhou, L., Xia, Y.-J., Shen, Y., Haselhuhn, A. S., Wegner, D. M., Li, Y.-B., & Carlson, B. E. (2021). Comparative study on resistance and displacement based adaptive output tracking control strategies for resistance spot welding. *Journal of Manufacturing Processes, 63*, 98–108. https://doi.org/10.1016/j.jmapro.2020.03.061

Zhou, L., Zheng, W., Li, T., Zhang, T., Zhang, Z., Zhang, Y., Wu, Z., Lei, Z., Wu, L., & Zhu, S. (2020). A material stack-up combination identification method for resistance spot welding based on dynamic resistance. *Journal of Manufacturing Processes, 56*, 796–805. https://doi.org/10.1016/j.jmapro.2020.04.051